

## New developments in micro-X-ray diffraction and X-ray absorption spectroscopy for high-pressure research at 16-BM-D at the Advanced Photon Source

Changyong Park, Dmitry Popov, Daijo Ikuta, Chuanlong Lin, Curtis Kenney-Benson, Eric Rod, Arunkumar Bommananvar, and Guoyin Shen

Citation: [Review of Scientific Instruments](#) **86**, 072205 (2015); doi: 10.1063/1.4926893

View online: <http://dx.doi.org/10.1063/1.4926893>

View Table of Contents: <http://scitation.aip.org/content/aip/journal/rsi/86/7?ver=pdfcov>

Published by the [AIP Publishing](#)

---

### Articles you may be interested in

[Preface: High-pressure studies with x-rays](#)

Rev. Sci. Instrum. **86**, 071901 (2015); 10.1063/1.4926899

[High-pressure, high-temperature x-ray absorption fine structure transmission cell for the study of aqueous ions with low absorption-edge energies](#)

Rev. Sci. Instrum. **75**, 5228 (2004); 10.1063/1.1813131

[Multichannel detector-collimator for powder diffraction measurements at energy scanning x-ray absorption spectroscopy synchrotron radiation beamlines for high-pressure and high-temperature applications](#)

Rev. Sci. Instrum. **74**, 2654 (2003); 10.1063/1.1568553

[Laser heated diamond cell system at the Advanced Photon Source for in situ x-ray measurements at high pressure and temperature](#)


Rev. Sci. Instrum. **72**, 1273 (2001); 10.1063/1.1343867

[An experimental station for advanced research on condensed matter under extreme conditions at the European Synchrotron Radiation Facility - BM29 beamline](#)


Rev. Sci. Instrum. **71**, 2422 (2000); 10.1063/1.1150631

---


Frustrated by old technology?



Is your AFM dead and can't be repaired?



Sick of bad customer support?




**It is time to upgrade your AFM**

Minimum \$20,000 trade-in discount for purchases before August 31st

**Asylum Research is today's technology leader in AFM**

[dropmyoldAFM@oxinst.com](mailto:dropmyoldAFM@oxinst.com)



# New developments in micro-X-ray diffraction and X-ray absorption spectroscopy for high-pressure research at 16-BM-D at the Advanced Photon Source

Changyong Park,<sup>a)</sup> Dmitry Popov, Daijo Ikuta, Chuanlong Lin, Curtis Kenney-Benson, Eric Rod, Arunkumar Bommananvar, and Guoyin Shen  
*High Pressure Collaborative Access Team, Geophysical Laboratory, Carnegie Institution of Washington, Argonne, Illinois 60439, USA*

(Received 22 February 2015; accepted 3 May 2015; published online 21 July 2015)

The monochromator and focusing mirrors of the 16-BM-D beamline, which is dedicated to high-pressure research with micro-X-ray diffraction (micro-XRD) and X-ray absorption near edge structure (XANES) (6–45 keV) spectroscopy, have been recently upgraded. Monochromatic X-rays are selected by a Si (111) double-crystal monochromator operated in an artificial channel-cut mode and focused to  $5\ \mu\text{m} \times 5\ \mu\text{m}$  (FWHM) by table-top Kirkpatrick-Baez type mirrors located near the sample stage. The typical X-ray flux is  $\sim 5 \times 10^8$  photons/s at 30 keV. The instrumental resolution,  $\Delta q/q_{\text{max}}$ , reaches to  $2 \times 10^{-3}$  and is tunable through adjustments of the detector distance and X-ray energy. The setup is stable and reproducible, which allows versatile application to various types of experiments including resistive heating and cryogenic cooling as well as ambient temperature compression. Transmission XANES is readily combined with micro-XRD utilizing the fixed-exit feature of the monochromator, which allows combined XRD-XANES measurements at a given sample condition. © 2015 AIP Publishing LLC. [<http://dx.doi.org/10.1063/1.4926893>]

## I. INTRODUCTION

The beamline 16-BM-D is one of four beamlines operated by the High Pressure Collaborative Access Team (HPCAT) at the Advanced Photon Source (APS) and is dedicated to high-pressure research in physics, chemistry, materials science, and earth and planetary sciences using micro-X-ray diffraction (micro-XRD), X-ray absorption spectroscopy (XAS), and anomalous X-ray scattering/diffraction.<sup>1</sup> The beamline has been optimized mainly for micro-XRD techniques since it became operational in 2006 and has made significant contributions to many areas of science, for example, pressure-induced phase transition,<sup>2–6</sup> structure determination,<sup>7–9</sup> structure and property correlation,<sup>10–13</sup> superconductivity,<sup>14–17</sup> and amorphous materials.<sup>18–21</sup> In the course of continuous development, many discoveries have been made, including high-pressure phases,<sup>22–28</sup> properties,<sup>29,30</sup> and processes.<sup>31,32</sup> Recently, the development of the single crystal X-ray diffraction (SXD) technique opened the door to studies of electron density distribution at high pressure,<sup>33</sup> and a new setup for XAS measurements has been successfully integrated and demonstrated.<sup>34,35</sup>

High-pressure XRD and XAS experiments require several critical conditions to be met by the instrumental setup. Fundamentally, the 16-BM-D beamline is designed to accommodate experiments conducted using diamond anvil cells (DACs), so the beam characteristics and sample/detector configurations are optimized to meet the constraints of the DAC environment. First, since the size of the sample in a DAC is typically 20–150  $\mu\text{m}$  in diameter and 5–40  $\mu\text{m}$  in

thickness, the incident X-ray beam must be finely focused to effectively scatter from the minute volume of the sample and also to avoid scattering from the gasket material (typically a metal). For the case of an extremely high pressure experiment (e.g., pressures greater than 100 GPa), the sample diameter is even further reduced to 5–30  $\mu\text{m}$  such that the confinement of the entire beam within the narrow gasket diameter becomes a critical requirement. Second, the use of thick diamond anvils (typically  $\sim 4$  mm total for a pair of anvils) causes significant attenuation of low energy X-rays so that the incident X-ray energy needs to be high enough to effectively penetrate through the anvils and minimize the attenuation correction. Bright, high-energy X-rays like those from the APS bending magnet source ( $E_c = 19.5$  keV)<sup>36</sup> are key to overcoming this limitation. Finally, high-pressure XRD and XAS studies are based on *in situ* characterization with various analytical approaches like phase identification, structure refinement, and property measurement under various sample environments including cryogenic cooling, resistive heating, fast compression, etc., so the setup needs to be versatile in order to match with the various combinations of experimental requirements. One of the most common but critical tests of this versatility, especially for XRD experiments, comes in achieving the proper compromise between real space and reciprocal space resolutions (i.e., maximum angle vs. angular resolution) for each experiment. The X-ray energy and the detector distance need to be adjustable, and the alignment must be both stable and reproducible.

The 16-BM-D micro-XRD setup is compatible with high pressure sample environments ranging from  $\sim 4$  K cryogenic cooling to 1000 K resistive heating, as well as room temperature compression. The powerful versatility comes from a combination of high-quality optical components and

<sup>a)</sup>Author to whom correspondence should be addressed. Electronic mail: [cpark@carnegiescience.edu](mailto:cpark@carnegiescience.edu)

reproducible alignment (on the order of a few  $\mu\text{m}$ ) and is essential for optimizing each individual experiment. Despite the frequent changes required to meet user requests, the beamline is operated in a fully optimized status. In parallel with user operations, new instrumental improvements are continuously under development.

Recently, the monochromator and the focusing mirrors were upgraded. The resulting improvements in instrumental characteristics essential to high-pressure micro-XRD experiments are described in this article. The recently added XAS setup gives 16-BM-D the unique capability of a push-button switchover between micro-XRD and XAS without disturbing the beamline alignment. Micro-XRD and XAS are powerful tools for studying materials' phases, structures, and properties. There is always an intimate relationship between the atomic and electronic structures; therefore, measuring both at identical pressure and temperature conditions provides better insight into the high-pressure properties. An example of a combined XRD-XANES measurement utilizing the exceptional reproducibility of the interchangeable setup is described in the later part of this article.

## II. BEAMLINE COMPONENTS AND PROPERTIES

### A. Layout

Figure 1 is a schematic of the beamline configuration with pictures of the major components of beamline, showing the Si (111) double-crystal monochromator in the 16-BM-C optical hutch, compact Kirkpatrick-Baez (KB) type focusing mirrors in the 16-BM-D experimental hutch, sample stage, and a large area detector. The monochromator is located roughly 40 m from the source and accepts beam through an entrance slit set to  $1.0\text{ mm} \times 1.0\text{ mm}$ . A second set of slits in front of the mirrors adjusts the footprint of the beam on the mirrors with a  $0.5\text{ mm} \times 0.5\text{ mm}$  aperture, which ultimately determines the available beam flux on the sample. The first mirror (vertical) is located 45 m from the source and the mirror length is 320 mm for both the vertical and horizontal mirrors. The

focal length of the second mirror to sample is around 0.5 m. After the focusing mirrors, a clean-up pinhole with  $\phi 25$ ,  $\phi 35$ , or  $\phi 75\text{ }\mu\text{m}$  size, depending on experimental requirements, is precisely aligned with respect to the focused beam center. The sample in a DAC can be compressed by a gear box (as shown in Fig. 1) or a gas diaphragm. An online ruby fluorescence spectrometer can be used to measure the sample pressure *in situ*. After the sample, a beamstop is aligned to block the direct beam. Finally, the X-ray diffraction pattern is collected using a large area detector (e.g., MAR345 Image Plate, CCD, PILATUS 1M, and Perkin-Elmer), which can be positioned from 0.3 m to 0.9 m downstream of the sample position.

### B. Energy calibration and resolution

The double crystal monochromator has a unique design which employs a low-torque sinebar rotation mechanism for changing the monochromator angle. The two crystals are aligned with each other in an artificial channel-cut geometry. The rotation center is off crystal to maintain a nearly fixed beam exit position with less than  $100\text{ }\mu\text{m}$  variation over an energy range of 6–60 keV.<sup>1</sup> The sinebar is pushed by a high-precision (20 nm resolution) stepper motor stage at the bottom of the chamber, which is carefully equilibrated with a spring mechanism to minimize changes in the pushing force over the full range of travel.<sup>37</sup> The entire chamber, including both crystal mount assembly and translation stage, is compact (L 0.5 m  $\times$  H 0.7 m  $\times$  W 0.8 m) and the components are ultra-high vacuum compatible. The monochromator crystals are cooled by circulating water at a constant temperature (e.g.,  $22.5^\circ\text{C}$ ).

Due to the unique mechanism for changing angle, the energy calibration of the monochromator is dependent upon several geometric factors: the length of sinebar ( $R_o$ ) and a fixed angular offset ( $\theta_o$ ) at the center of the translational stage travel ( $x_o$ ) (inset of Fig. 2(a)),

$$E(x) = \frac{hc}{2d\gamma_o} \cdot \frac{1}{\sin\left(\theta_o + \arctan\left(\frac{x-x_o}{R_o}\right)\right)}. \quad (1)$$

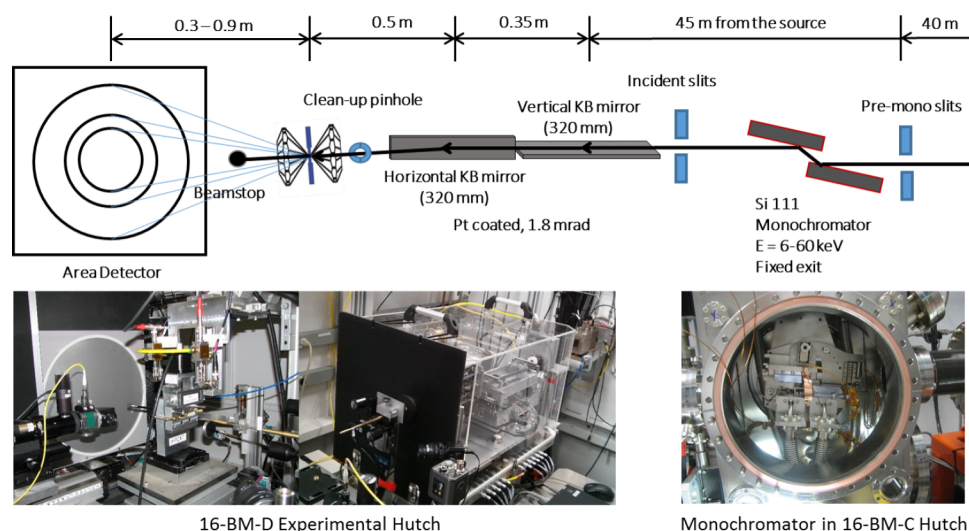


FIG. 1. Schematic layout and photographs of 16-BM-C and 16-BM-D beamline components.

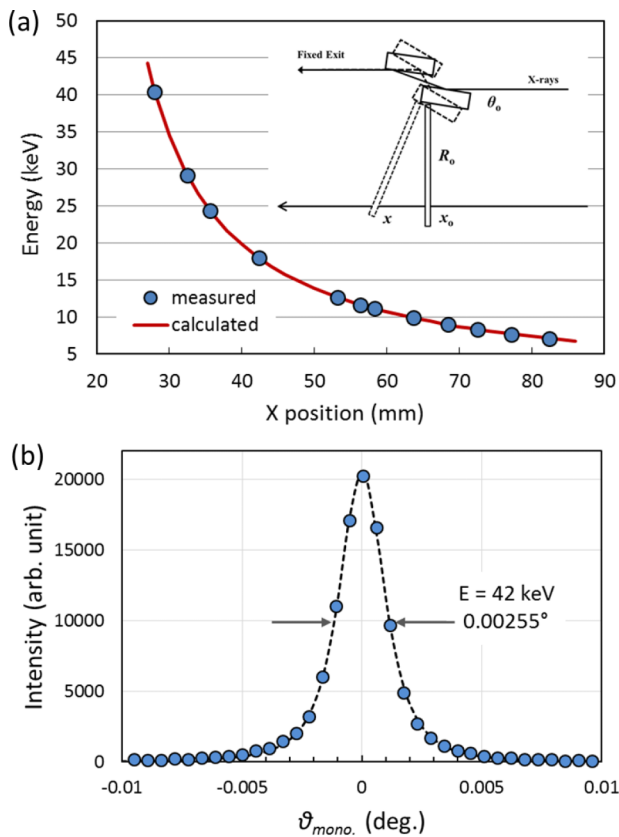


FIG. 2. (a) Schematic of fixed exit monochromator in artificial channel-cut mode (inset) and its energy calibration using known standard absorptions (EXAFS Materials). The incident angle on the first monochromator crystal, which determines the exit energy, is geometrically determined by the four parameters ( $\gamma_0$ ,  $x_0$ ,  $R_0$ , and  $\theta_0$ ; Eq. (1)). The second monochromator pitch can be adjusted for detuning. (b) The second monochromator rocking scan at  $E = 42$  keV (solid circles) and the Pearson VII profile fitting (dotted line). The estimated FWHM and  $m$ -exponent are  $0.00255^\circ$  (or  $44.5 \mu\text{rad}$ ) and  $1.593$ , respectively.

Here,  $h$  is Planck's constant,  $c$  is the speed of light,  $d$  is the  $d$ -spacing of Si (111) ( $3.1355 \text{ \AA}$ ), and  $\gamma_0$  is the thermal expansion correction. As shown in Fig. 2(a), the monochromator energy calibration can be obtained semi-permanently as a function of the translator  $x$ -position by fitting several measured energy points (EXAFS Materials standard foils) with  $\gamma_0$ ,  $\theta_0$ ,  $x_0$ , and  $R_0$  as the adjustable parameters. The average of the residual errors in the fitting corresponds to  $|\Delta E/E|_{\text{avg}} = 1.1 \times 10^{-4}$ .

The real energy resolution is obtained by convoluting the beam divergence with the Darwin width of the monochromator crystal. Assuming a point source for simplicity, the beam divergence is purely geometric, defined by the slit opening (1.0 mm in vertical) and the distance from the source (40 m, Fig. 1). The resultant energy resolution is expressed as  $\Delta E/E = \cot \theta_m \cdot \sqrt{(\Delta^2 \theta_S + \Delta^2 \theta_m)}$ , where  $\theta_m$  is the monochromator angle,  $\Delta \theta_S$  is the geometric beam divergence, and  $\Delta \theta_m$  is the Darwin width of the monochromator single crystal. The energy resolution broadened by this purely geometric factor can be readily calculated and a few examples are summarized in Table I. Note that  $\theta_m$  and  $\Delta \theta_m$  are energy dependent.

Figure 2(b) shows an example of the actual angular divergence of the second monochromator rocking scan at  $E = 42$  keV, where the measured FWHM ( $0.00255^\circ$  or

TABLE I. The energy resolution at different incident energy resulting from the convolution of intrinsic Darwin width of Si 111 reflection and the geometric beam divergence by slits,  $\Delta \theta_S = 25 \mu\text{rad}$ , for 16BM-C monochromator and the correction for the measured rocking scan width.

Energy (keV)	Monochromator angle $\theta_m$ (degrees)	Darwin width $\Delta \theta_m$ ( $\mu\text{rad}$ )	$\Delta E/E = \cot \theta_m \cdot \sqrt{(\Delta^2 \theta_S + \Delta^2 \theta_m)}$	$\Delta E/E \times 1.7$
24	4.73	10.7	$3.29 \times 10^{-4}$	$5.6 \times 10^{-4}$
30	3.78	8.54	$4.00 \times 10^{-4}$	$6.8 \times 10^{-4}$
42	2.70	6.09	$5.46 \times 10^{-4}$	$9.3 \times 10^{-4}$

$44.5 \mu\text{rad}$ ) corresponds to  $\sim 1.7$  times the geometrically broadened width ( $0.00147^\circ$  or  $25.7 \mu\text{rad}$ ). The measured rocking scan width is a result of convolution of the geometric divergence, two monochromator crystals, and the intrinsic source divergence, i.e.,  $\sqrt{(\Delta^2 \theta_S + 2\Delta^2 \theta_m + \Delta^2 \theta_{\text{source}})}$ . The corresponding source divergence and/or possible peak broadening due to imperfections in the monochromator crystals is estimated to be  $35 \mu\text{rad}$ . Applying this empirically determined broadening factor of 1.7 to the theoretical geometric broadening yields the values listed in the last column of Table I. The linearized trend predicts  $(\Delta E/E)_{\text{practical}} = 5 \times 10^{-4}$  at  $E = 20$  keV and  $1 \times 10^{-3}$  at  $E = 45$  keV, respectively, for example.

### C. Focused beam profile

The monochromatic beam is focused by a pair of table-top compact KB mirrors (Instrument Design Technology) located in the 16-BM-D experimental hut (Fig. 1). The mirror substrate is made of single crystal Si and the surface is coated with two metal stripes, Pt and Rh, to provide options in mirror angles and cut-off energies. The mirrors are tapered and mounted on a tapered-mirror-bender system.<sup>38,39</sup> The mirrors and bender system are enclosed in a He gas filled chamber. The dimensions of the chamber are  $L 0.7 \text{ m} \times H 0.5 \text{ m} \times W 0.5 \text{ m}$  and a leaded shield on the downstream face protects the sample/detector area against background scattering from the mirrors (the black panel in the picture in Fig. 1).

For the normal operation, the Pt stripe is used at  $1.8 \text{ mrad}$  incidence angle. Since the useable length of mirror is approximately 280 mm, the effective beam cross section is limited to 0.5 mm. The slit sizes are set to match this cross-sectional limit and the mirror centers are precisely aligned with respect to the slits. The cut-off energy is around 47 keV, which gives enough room for the normal operation range of energy (6–45 keV). The cutoff can be extended to higher energy up to 60 keV by changing the mirror angles and the slit sizes at the cost of incident beam intensity. This high-energy operation is infrequent but can be readily configured to meet the experimental demands.

Figure 3 shows the focused beam profiles measured by an edge scan with a tungsten-rod. In both the vertical and horizontal directions, the focused beam has  $4.5 \mu\text{m}$  FWHM, while the tail width (defined by the point at which the intensity drops to  $<1\%$  of the peak) is  $\sim 30 \mu\text{m}$  for vertical and  $\sim 15 \mu\text{m}$  for horizontal profiles, respectively. Since the beam divergence slightly changes at different energies, the



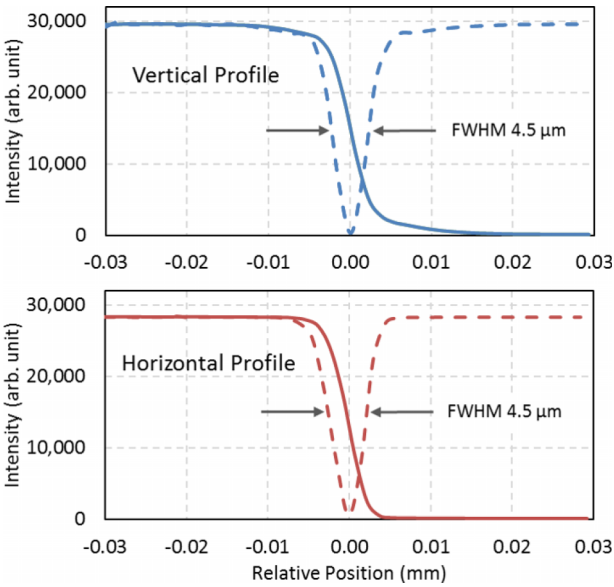


FIG. 3. Focused beam profiles scanned by a tungsten rod and their derivatives in the vertical (top) and horizontal (bottom) directions, respectively.

final focal shapes also change with energy. Table II presents selected examples of the focal size changes with different values of energy, mirror angle, and incident slit size.

D. Incident beam intensity

The flux (photons/s) of the focused beam immediately after the clean-up pinhole was measured using a gas ion chamber (ADC MIC-205) detector, and the results are presented in Fig. 4 (blue circles). The errors are estimated to be approximately 10%. At each energy, the pitch of the second monochromator crystal was re-optimized to maximize the intensity after the pinhole and the focal size was also refined; therefore, the uncertainties are mainly from possible misalignment of the optical components. The 10% errors are arbitrary rather than systematic and are conservative compared to the electronic noise in the detector counts, which is typically far less than 1%.

The maximum flux after the pinhole is obtained at around 20 keV, which is consistent with the known critical energy of the APS bending magnet ( $E_C = 19.5$  keV).<sup>36</sup> The absolute photon count rate is  $\sim 8 \times 10^8$  photons/s, which corresponds to  $\sim 3 \times 10^7$  (photons/s)/ $\mu\text{m}^2$  at the  $5 \mu\text{m} \times 5 \mu\text{m}$  focal point. The photon flux at the sample is largely limited by the focusing mirrors, more specifically the useable mirror length and angle.

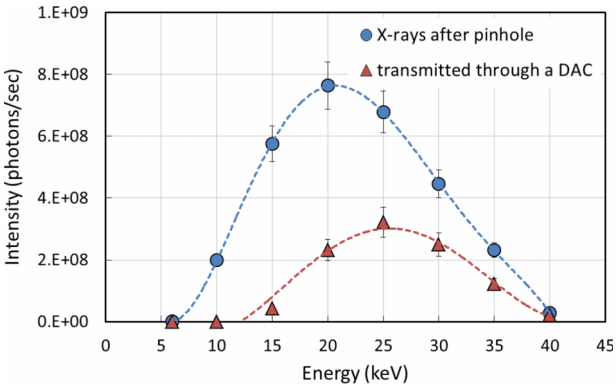


FIG. 4. X-ray intensity after the pinhole (blue circles) and the effective intensity (red triangles) corrected for air, diamond, and sample attenuations.

The incident beam cross-sectional area ( $0.5 \text{ mm} \times 0.5 \text{ mm}$ , see the Section II C) for the mirrors is the major factor in this limitation. The efficiency for two mirrors is  $\sim 0.8$  over 20–40 keV energy range for the Pt coated stripe at 1.8 mrad angle. The flux before the mirrors and after the  $0.5 \text{ mm} \times 0.5 \text{ mm}$  slit is  $\sim 1 \times 10^9$  photons/s.

When the practical factors like air attenuation, absorption by the diamond anvils and sample (especially in a material including heavy elements), and the detector efficiency are considered, the effective intensities measured below 20 keV energy are dramatically suppressed and the effective maximum intensity point shifts toward 25 keV (red triangles in Fig. 4). If the maximum angle necessary for a particular diffraction experiment is considered, the optimal incident energy can shift even higher. In practice, the majority of experiments at the 16-BM-D are performed at 30 keV as a compromise between intensity and  $q$ -range. Higher energies approaching 40 keV are also frequently used for collecting more diffraction lines (or more single crystal peaks), depending on the experimental requirement.

The high photon flux at the focal point (i.e.,  $\sim 3 \times 10^7$  (photons/s)/ $\mu\text{m}^2$ ) is one of the key characteristics required for high-pressure X-ray diffraction experiments using diamond anvil cells, for which the samples are typically loaded in a gasket hole less than  $200 \mu\text{m}$  in diameter and  $40 \mu\text{m}$  in thickness. The finely focused beam is not only required for scattering efficiency (i.e., the entire beam irradiates the sample) but also is useful to enhance the signal-to-noise ratio. However, powder samples with poor size distribution (e.g., too many grains above  $\phi 1 \mu\text{m}$ ) can suffer from the small beam size. In that case, the beam can be intentionally defocused or the data can be collected by summing a raster of sample

TABLE II. Selected examples of beam focus with different energies, angles, and slit sizes.

Energy	40 keV		29.2 keV			
Angle	1.8 mrad		2.0 mrad			
Slits	0.5 mm $\times$ 0.5 mm		0.52 mm (v) $\times$ 0.56 mm (h)		0.3 mm $\times$ 0.3 mm	
Widths	FWHM ( $\mu\text{m}$ )	Full <sup>a</sup> ( $\mu\text{m}$ )	FWHM ( $\mu\text{m}$ )	Full ( $\mu\text{m}$ )	FWHM ( $\mu\text{m}$ )	Full ( $\mu\text{m}$ )
Vertical	5.0	30	4.9	27	4.0	27
Horizontal	5.0	15	4.4	11	3.2	11

<sup>a</sup>Full width at 1% maximum.

positions to keep a few large grains from dominating the diffracted intensity pattern.

### E. Clean-up pinhole

The clean-up pinhole plays a critical role in suppressing background noise by confining the incident beam within the sample gasket hole, thereby avoiding X-rays scatter from unwanted sources (e.g., metal gasket diffraction). In principle, a smaller pinhole closer to the sample is better in terms of efficacy. However, the sample-pinhole distance cannot always be small but must allow for various sample environment equipment (e.g., cryostat). A series of pinholes with various sizes ( $\phi 25$ ,  $\phi 35$ , or  $\phi 75$   $\mu\text{m}$ ) and precision stages to align them with the incident beam are required to properly collimate the incident beam for all experiments. The largest pinhole ( $\phi 75$   $\mu\text{m}$ ), employed in the range of 25 mm to 75 mm from the sample, is the most frequently used at 16-BM-D for various experimental conditions ranging from cryogenic cooling to resistive heating and for diffraction experiments combined with X-ray absorption spectroscopy.

## III. INSTRUMENTAL BROADENING AND RESOLUTION

### A. Peak broadening

The X-ray diffraction pattern is collected by a large flat area detector in a forward scattering geometry (Fig. 1), for

which the Debye-Scherrer cones (from powder samples) or single crystal peaks are detected within a certain limited diffraction angle. To increase the maximum  $q$ , defined as  $(4\pi/\lambda) \sin \theta$ , where  $\lambda$  is the X-ray wavelength and  $\theta$  is a half of the  $2\theta$  diffraction angle, the detector is often placed as near as possible to the sample and/or the X-ray energy is chosen as high as possible (e.g., around 40 keV or above). In contrast, to configure the finest instrumental resolution, the detector distance is adjusted to be reasonably far from the sample and/or the X-ray energy is chosen as low as possible (e.g., around 25 keV, which is also consistent with the maximum intensity condition as suggested in Fig. 4). The discrete pixel resolution of the large area detector and the detector efficiency as function of energy are also factors to be considered in the data collection optimization. This adaptability is essential to the execution of various high-pressure XRD experiments; however, the trade-off is a loss of constant instrumental characteristics, which necessitates systematic evaluation for many different experimental conditions.

Figure 5 is an example of a 2D X-ray diffraction pattern from  $\text{CeO}_2$  standard powder (NIST SRM 674b) measured using a MAR345 Image Plate detector at  $\sim 310$  mm sample-to-detector distance and  $E = 40.000$  keV, and its corresponding 1D diffraction pattern integrated after a geometric correction using Fit2d software.<sup>40</sup> The angular distribution of the measured data points (red asterisks) is based on the sampling, with a discrete 100  $\mu\text{m}$  pixel size, of the area detector at the

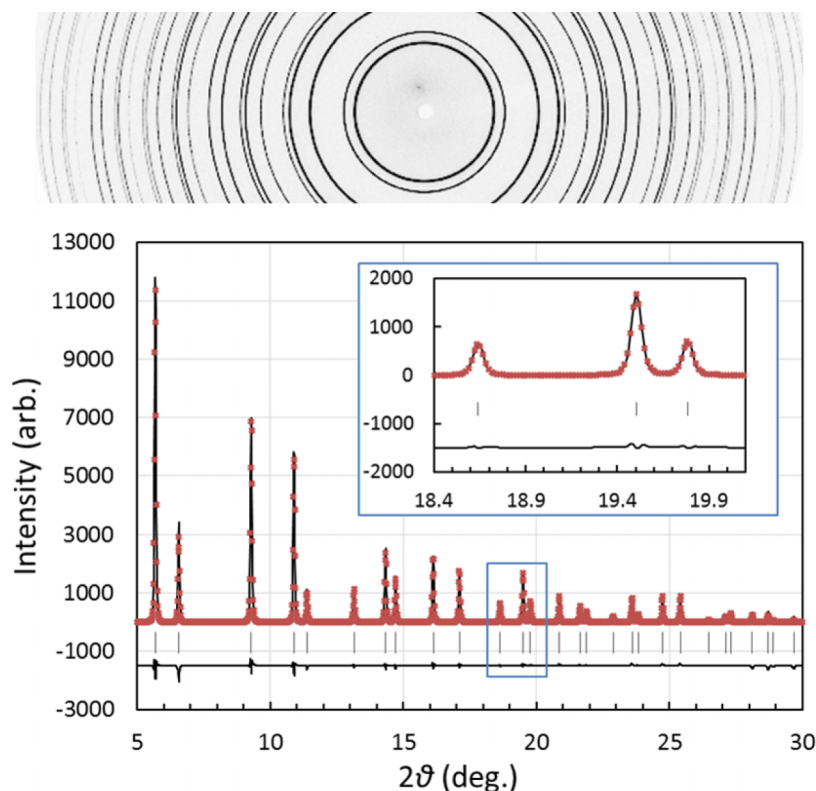


FIG. 5. An example of 2D XRD image (cropped) from  $\text{CeO}_2$  standard powder (NIST SRM 674b) and its corresponding 1D diffraction pattern (red asterisks) integrated along the azimuthal direction after the geometric correction using Fit2d software.<sup>40</sup> The solid line is a result of full profile fitting with the Pearson VII function for which the exponent ( $m$ ) and the  $U$ ,  $V$ , and  $W$  parameters of the Caglioti function are pre-defined as in Fig. 6. The overall scale factor, background profile, wavelength, and isotropic thermal vibration amplitude are adjusted to better match with the measured data. The inset shows the typical peak shape and an example of the best quality of fit.

particular distance. The solid line represents the result of a full profile fitting using FULLPROF<sup>41</sup> after subtracting the background. The inset shows the typical peak shape and an example of the best quality of fit reproducing the measured data.

In the full profile fitting, the peak shape was approximated by the Pearson VII function, which is chosen to be consistent with that used to evaluate the monochromator rocking scan curve (Fig. 2(b)). The shape parameter ( $m$ ) of the Pearson VII function and the U, V, and W parameters of the Caglioti function<sup>42</sup> were fixed with the pre-estimated values using the individually fitted peaks (see below). The overall scale factor, background profile, diffractometer center, wavelength, and isotropic thermal vibration amplitude were adjusted to fit the measured data.

The observed peak shape and width is a result of the convolution of source divergence, monochromator dispersion (Fig. 2(b)), effect of beam focusing,<sup>43</sup> intrinsic peak width due to particle size and strain of the sample,<sup>42</sup> and pixel resolution of the area detector. Assuming a Gaussian convolution, the total FWHM is obtained as  $FWHM^2(2\theta) = \Delta^2(2\theta)_{\text{source\&mono}} + \Delta^2_{\text{mirror}} + \Delta^2(2\theta)_{\text{sample}} + \Delta^2_{\text{detector}}$ , where  $\Delta(2\theta)_{\text{source\&mono}} \approx 2 \tan \theta / \tan \theta_m \cdot \sqrt{(\Delta^2 \theta_S + 2\Delta^2 \theta_m)}$  and  $\Delta_{\text{mirror}} \approx \sqrt{(\frac{A_o}{D_H D_V})}$ , where  $A_o$  is the cross sectional area of the incident beam (i.e., slit area) onto the mirror and  $D_H$  and  $D_V$  are the mirror to sample distance in horizontal and vertical direction, respectively,  $\Delta(2\theta)_{\text{sample}} \approx 0.9\lambda / (L \cos \theta) + \varepsilon \cdot \tan \theta$  from the Hall-Williamson equation, and  $\Delta_{\text{detector}} \approx l_p / D_D$ , where  $l_p$  is the pixel size and  $D_D$  is the sample to detector distance. From Section II B,  $\Delta(2\theta)_{\text{source\&mono}}$  will vary from  $\sim 0.005^\circ$  to  $\sim 0.025^\circ$  due to the factor  $\tan \theta$  when  $2\theta$  approaches  $\sim 30^\circ$ . The geometrically averaged divergence due to the mirror focusing is around  $0.044^\circ$ , which is the largest contribution to the peak broadening. The average particle size of the NIST CeO<sub>2</sub> powder (RSM 674b) is known to be  $\sim 380$  nm, which influences the peak broadening by  $\sim 0.0042^\circ$ , and the effect of strain is negligibly small. The detector's pixel size is known (e.g., 0.1 mm for the highest resolution in case of MAR345 Image Plate detector, 0.2 mm for Perkin-Elmer, and 0.172 mm for Pilatus detector) so that the pixel resolution is merely an inverse function of the sample to detector distance, which can make a significant contribution to the peak width. For example, at  $D_D = 660$  mm,  $\Delta_{\text{detector}} = 0.0087^\circ$  for MAR345 Image Plate detector at the highest resolution mode, and  $\Delta_{\text{detector}} = 0.017^\circ$  at  $D_D = 330$  mm.

While the above approximation still represents an ideal case, the peak broadening is non-ideal in most cases and must be practically determined. Figure 6 shows selected examples of peak broadening and shape variation in various cases with the CeO<sub>2</sub> standard powder measured by a MAR345 IP detector at two different detector distances and at three different incident energies. Here, the shape parameter (the  $m$ -exponent of the Pearson VII function) variations are approximated with a parabolic function of  $2\theta$ , and the FWHM is approximated with the Caglioti function,<sup>42</sup>  $\Delta^2(2\theta) = U \tan^2 \theta + V \tan \theta + W$ . In Fig. 6(a), the observed peak widths measured at  $D_D = 660$  mm and  $E = 40$  keV appear around  $0.044^\circ$ – $0.047^\circ$ , which correspond to nearly

ideal values based on the given geometric factors above. In contrast, the peak widths in Figs. 6(b)–6(d) measured at  $D_D = 330$  mm show  $\Delta(2\theta) \approx 0.06^\circ$  and greater regardless of the incident X-ray energy, which are significantly larger values than those expected from the known geometric factors and which indicate that another significant peak broadening process (e.g., point spread function) might be involved in the measurement. Since all four cases show different shape variations in the parabolic approximation, the possible source of the excess broadening may include a subtle misalignment in the optical components during the switch between different configurations. However, the peak width variation is relatively consistent, especially when the detector distance is fixed (Figs. 6(b)–6(d)), which confirms the stability of alignment with large changes in the X-ray energy.

## B. Instrumental resolution

The instrumental resolution is expressed with  $\Delta\theta \cot \theta$ , which is equivalent to  $\Delta q/q$ . In Fig. 7, a series of  $\Delta q/q$  plots are shown for various combinations of detector pixel size, detector distance, and incident X-ray energy. For each set of data, a constant  $\Delta q$  was estimated for the comparison. Among these tested diffractometer setups, the finest  $\Delta q/q$  is obtained when the incident energy is set around  $\sim 24$  keV at the cost of the maximum  $q$ , which is limited to around  $5 \text{ \AA}^{-1}$ . On the other hand, the highest maximum  $q$  is obtained at around  $10 \text{ \AA}^{-1}$ , when the incident energy is set near 40 keV and the detector distance is 330 mm. The advantage of the latter case is obvious but a toll is paid in the instrumental resolution, where  $\Delta q$  is almost twice the finest resolution.

While both high resolution and maximum  $q$ -range must be taken into account, the most relevant measure of the diffractometer performance is its applicability to the experiment at hand. Resolution is critical for some experiments such as identification of subtle phase transitions (e.g., cubic to distorted cubic or tetragonal phase transition) and structure refinement of low symmetry materials, but many high-pressure XRD experiments do not require the finest resolution. Most experiments will need a compromise between these two requirements, which can be found around  $E \approx 30$  keV and  $D_D \approx 330$  mm (green circles in Fig. 7). In general, the 16-BM-D XRD setup is adaptable for various experimental requirements, and Figure 7 provides a useful guide to choose the right instrumental setup for each type of experiment.

## IV. DEVICE SETUP REQUIRED FOR HIGH-PRESSURE STUDIES

High-pressure experiments simultaneously involve many complementary devices, including remotely controlled pressure devices (gearbox, gas diaphragm, etc.), temperature devices (cryostat, resistive heater, etc.), and *in situ* pressure and temperature monitors. These devices add substantial weight to the experimental table. The impact is significant and a heavy duty sample stage is an essential component for a versatile application of the beamline to various high-pressure studies. The heavy-duty sample stage stack, from

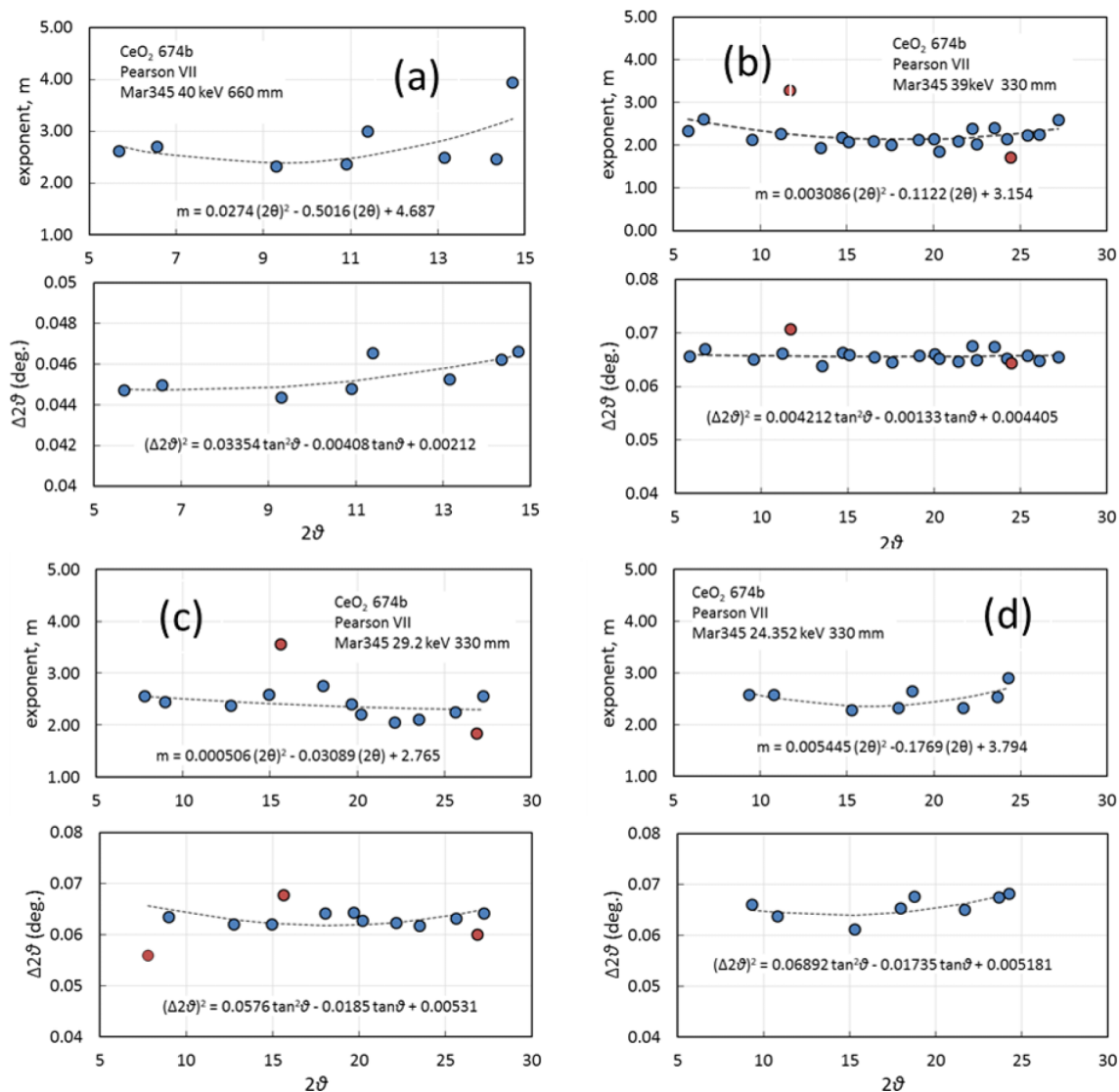


FIG. 6. The peak width variations in the diffraction pattern from the CeO<sub>2</sub> powder (NIST RSM 674b) measured at various combinations of X-ray energies and the detector distances: (a) E = 40 keV and D<sub>D</sub> = 660 mm, (b) E = 39 keV and D<sub>D</sub> = 330 mm, (c) E = 29.2 keV and D<sub>D</sub> = 330 mm, and (d) E = 24.352 keV and D<sub>D</sub> = 330 mm. MAR345 Image Plate detector with 100 μm discrete pixel size was used. Each individual peak was pre-evaluated with the Pearson VII function. The trends in the exponent (m) and the FWHM (dashed lines) are based on the models  $m = a(2\theta)^2 + b(2\theta) + c$  and  $\text{FWHM}^2 = U \tan^2 \theta + V \tan \theta + W$ , respectively. The outlier data points (not used in the fitting) are expressed by red color. The equations are expressed with the best fit parameters.

top to bottom, consists of high-precision XY translators (0.25 μm stepping), rotation stage (0.001° precision), Z translator (0.02 μm stepping), and another XY translator stage at the bottom (0.25 μm stepping). The diffractometer's 2θ center can be precisely aligned to the focused beam center within a micrometer using these high-precision heavy-duty stages.

These stages fill a large volume and place limitations on critical dimensions like the clean-up pinhole to sample distance and detector distance. For example, the closest pinhole position is limited to 75 mm for cryogenic experiments, compared to 25-30 mm for a normal DAC in a room temperature experiment and 40-50 mm for a resistively heated DAC. During such experiments that require temperature control, an on-line ruby fluorescence system must be used to measure the sample pressure without disturbing the alignment of the DAC. The system is mounted on a motorized stage to facilitate

its removal from the beam path and diffraction image area (Fig. 1), but the system inevitably requires space between the sample and the beam stop, thus limiting the closest approach of the detector to the sample position. Currently, the smallest achievable distance between the detector and diffractometer at the 16-BM-D is around 300 mm. However, this limitation is made up for by the ability to add on-line Raman spectroscopy or portable laser-heating systems, since the space required for these additional instruments already exists in the current layout.

Some typical experimental setups at the 16-BM-D beamline include remote pressure control using either high-precision gear-box or gas diaphragm, resistive heating up to 1000 K, cryogenic cooling to 4 K, on-line Raman spectroscopy, and portable laser heating. Note that the techniques for remote pressure and temperature control must be accompanied by the *in situ* pressure calibration and temperature



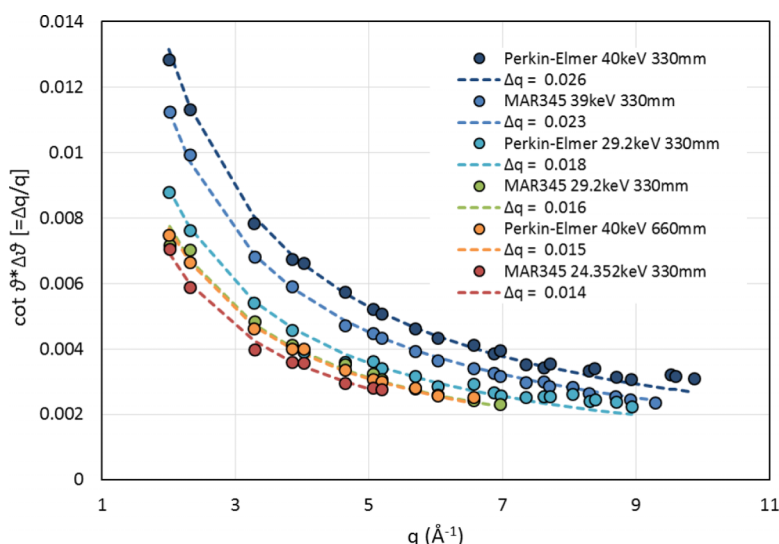


FIG. 7. Instrumental resolutions,  $\Delta q/q$ , evaluated using the  $\text{CeO}_2$  standard powder (NIST RSM 674b) with various combinations of detector choice, distance, and X-ray energy.

monitoring techniques. Many combinations of these instruments are possible, making 16-BM-D extremely versatile for various types of high-pressure experiments.

## V. X-RAY ABSORPTION SPECTROSCOPY COMBINED WITH MICRO-XRD

### A. Interchangeable XRD and XAS setup

The 16-BM-C monochromator is capable of performing X-ray absorption spectroscopy measurements. The total amount of vertical shift of the exit beam over  $E = 6\text{--}60$  keV is around  $100\text{ }\mu\text{m}$  (or  $\sim 2\text{ }\mu\text{m}$  per 1 keV);<sup>37</sup> therefore, a post-monochromator slit with a properly adjusted offset relative to the pre-monochromator slit can produce a fixed exit configuration. Even further, it is possible to combine the XAS measurement with XRD without changing the sample alignment, which opens up a new way to study the correlation between crystal structure and electronic structure under high-pressure.

The combined XRD-XAS measurement involves two different instrumental setups simultaneously, i.e., one for XRD and the other for XAS, which are easily interchangeable with each other. The XRD setup is a default setup and then the XAS setup is made by simply moving the monochromator position to the targeted absorption edge and scanning. Changing the energy does not disturb the instrumental characteristics as shown in Section III. The achromatic focusing optics alleviate the need to re-focus the beam at different energies but the second monochromator pitch angle must be adjusted to maximize the intensity after the pinhole. To monitor the incident X-rays and detect the transmitted X-rays before and after the sample, respectively, custom-designed low-profile gas ion-chambers (Advanced Design Consulting) are used. Pure Ar and Xe gases are typically used to increase the detection sensitivity at high energy above 20 keV and pure  $\text{N}_2$  gas or air is used for lower energy. The ion chambers are mounted on a pneumatically controlled stage (Fig. 1), which

allows changes between the XRD and the XAS measurements without having to access the experimental hutch.

### B. “Diamond glitches” and practical methods at 16-BM-D

X-ray transmission with varying energy through a single crystal diamond anvil causes a phenomenon known as a “diamond glitch.” The cause is the change in size of the Ewald sphere in reciprocal space when the incident X-ray energy is increased or decreased (Fig. 8(a)). Whenever the diffraction condition is fulfilled, a significant portion of the incident beam is diffracted by the single crystal diamond out of the direct beam, which disturbs  $I/I_0$  normalization and consequently the X-ray absorption spectrum with severe artifacts. This phenomenon becomes more profound at higher energy as the size of Ewald sphere is bigger, and hence, the probability to satisfy the diffraction condition is higher.<sup>44</sup>

To avoid diamond glitches, multiple practical approaches have been developed that can be implemented during the measurement. First, the sample orientation (more precisely the DAC orientation) can be delicately adjusted to shift the positions of obvious glitches in the spectrum and later manually cutting out the contaminated portion after finishing the data collection. By repeating the measurement with different sample orientations, the multiple spectral fragments with partially incomplete portions can be statistically averaged to obtain a reasonable full spectrum. This method can be applied to relatively low energy XAS, where the number of glitches is small and rotation of sample does not cause new glitches which otherwise would not appear. The downside is that this method requires a large amount of time and post-process effort.

Second, using the recently developed nano-polycrystalline-diamond (NPD) anvils, a “glitch-free” absorption spectrum can be measured.<sup>44</sup> This method is the most effective and convenient approach to solve the diamond-glitch problem except for the case, especially problematic for the combined

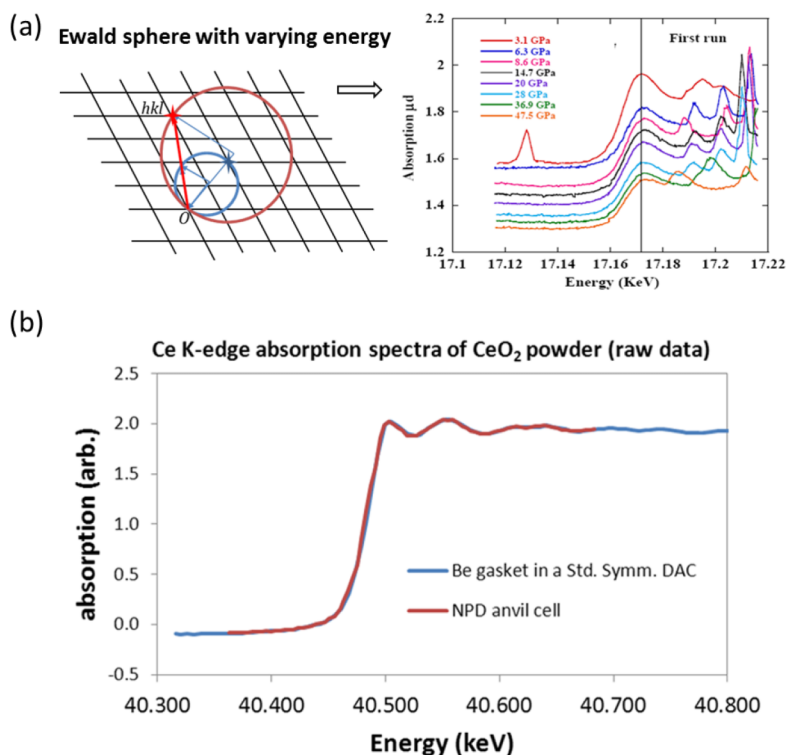


FIG. 8. (a) Schematic of Ewald sphere construction for single crystal diamond diffraction with varying X-ray energies and an example of the resultant “diamond glitches” ruining the XAS’ spectra. (b) Comparison of Ce K-edge XANES spectra from CeO<sub>2</sub> powders in a nano-polycrystalline diamond anvil cell in normal on-axis geometry and a standard symmetric DAC with beryllium gasket in radial transmission geometry, respectively, showing identical results.

XRD-XAS study, where the XRD pattern of NPD happens to overlap with that of the sample. For the application at an energy lower than  $\sim 20$  keV (see Fig. 4), the anvil needs to be properly perforated to reduce the X-ray attenuation caused by thick NPD anvils.

Third, one can utilize an X-ray transparent beryllium gasket in radial transmission and diffraction geometry or combine the radial transmission geometry for XAS and the normal on-axis geometry for XRD measurement by rotating the sample  $90^\circ$  for each interchanged setup. This method involves intense sample stage operation and requires a precise alignment of the sample rotation center. The advantage is that the beryllium gasket technique is well established in the high-pressure community and the materials are readily available. The disadvantage is that the gasket is so soft that the sample thickness may change with increase of pressure, which can cause a systematic shift in the normalized absorption. Figure 8(b) directly compares the second (NPD anvil) and the third (Be gasket in radial transmission geometry) cases, which result in identical absorption spectrum. Compared to the first approach, the second and the third approaches are relatively reliable and often used at 16-BM-D.

### C. An example of combined XRD-XANES study

Pressure-induced isostructural volume collapse is an intriguing phenomenon and much attention has been paid to the electronic mechanisms that drive it.<sup>45–52</sup> Praseodymium is a rare earth element that shows such a collapse,<sup>53,54</sup> and similar behavior in its hydride compound (PrH<sub>2</sub>) is of primary interest in this study.

The combined XRD-XANES measurements for a PrH<sub>2</sub> powder sample under compression were performed at 16-BM-D. The powder sample was loaded into an  $\sim \phi 80$   $\mu\text{m}$  beryllium gasket hole in a DAC with  $\phi 400$   $\mu\text{m}$  culet in the HPCAT glove box. Sealed in the Ar environment of the glove box, the pressure medium was replaced with neon using the GSECARS gas-loading system. The XRD and XANES data were collected as a set for each pressure point. The pressure was increased using a gas diaphragm and monitored *in situ* using an online ruby fluorescence system. The XRD was measured at  $E = 36.000$  keV in normal on-axis geometry through the diamond anvils, while the XANES was measured at the Pr K-edge (41.991 keV) in radial transmission geometry through the beryllium gasket after rotating the sample by  $90^\circ$ . The rotation center of the sample was aligned within 2  $\mu\text{m}$  precision in terms of the sphere of confusion. The XRD-XANES measuring cycle was repeated for every pressure point selected between 1.7 GPa and 30.4 GPa. The pressure control and the setup exchange were remotely controlled, which allowed the entire data set to be obtained in one session (i.e., no hutch access and no interruption of measurement).

Figure 9(a) is the summary of the powder XRD of PrH<sub>2</sub> with pressure and Fig. 9(b) is the corresponding XANES spectra at the same pressure points. In Fig. 9(a), the high-density fcc phase appears at 11.7 GPa and the low-density fcc phase continues to be seen even at the highest pressure of 30.4 GPa in this study. The vertical bars at the bottom and the top indicate the fluorite structure fcc peak positions of a low density phase and a high density phase, respectively. The coexistence of the low and high-density phases and the

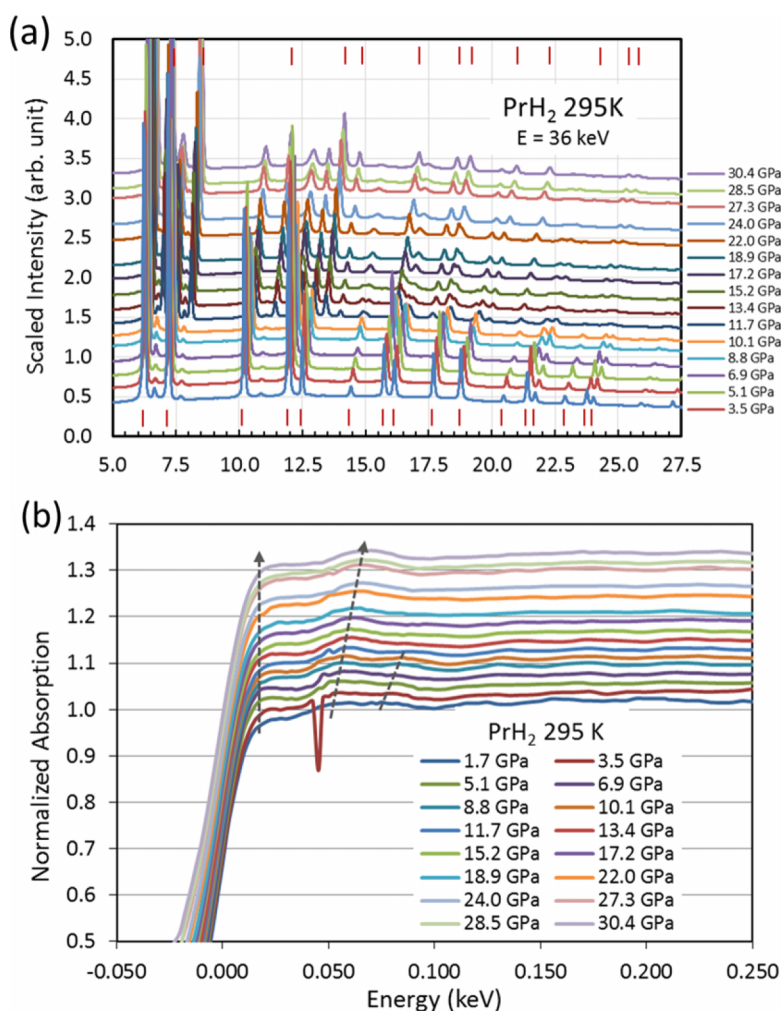


FIG. 9. (a) XRD patterns with pressure at room temperature from  $\text{PrH}_2$  powder in a standard symmetric DAC and (b) normalized XANES spectra at identical sample conditions. For each pressure point, the XRD was measured in normal on-axis geometry and the XANES was measured in radial transmission geometry by rotating the sample DAC by  $90^\circ$  to allow the incident beam pass through the beryllium gasket.

gradual transition between them is observed over a range of 20 GPa. However, completion of the phase transition (i.e., higher pressure data) could not be observed in this particular set of measurements due to thinning of the soft gasket material.

The raw data of the XANES spectra were normalized using Athena software<sup>55</sup> and the relative variations in the whiteline features were aligned with respect to the experimental absorption edge (Fig. 9(b)). Due to the short length of the ion chambers needed to perform this experiment, the XANES data generally suffer from a low signal to noise ratio. Nevertheless, a systematic variation with the increase of pressure is observed, indicated by the two arrows over the first whiteline peaks and the second whiteline peaks, respectively. Relative to the reference position of the first whitelines, the second whiteline peaks show a distinct linear shift with pressure. Compared to the appearance of the high-density fcc phase found in the XRD pattern, the XANES pattern does not show a distinct peak or a dramatic change indicating the isostructural volume collapse. Instead, the originally enriched oscillatory features seen in the low density phase up to 10.1 GPa disappear, likely smeared out by mixing of the two phases. A short dashed line is added to indicate the third peak

trend, which stops at 10.1 GPa. The muted signals, however, reflect the weak sensitivity of the K-edge absorption process of Pr to the electronic transition accompanying the structural transition. Further analysis is required to fully describe the observations.

## ACKNOWLEDGMENTS

The experiments were performed at HPCAT (Sector 16), Advanced Photon Source (APS), Argonne National Laboratory. HPCAT operations are supported by DOE-NNSA under Award No. DE-NA0001974 and DOE-BES under Award No. DE-FG02-99ER45775, with partial instrumentation funding by NSF. Use of the COMPRES-GSECARS gas loading system was supported by COMPRES under NSF Cooperative Agreement No. EAR 11-57758 and by GSECARS through NSF Grant No. EAR-1128799 and DOE Grant No. DE-FG02-94ER14466. The Advanced Photon Source is a U.S. Department of Energy (DOE) Office of Science User Facility operated for the DOE Office of Science by Argonne National Laboratory under Contract No. DE-AC02-06CH11357. We thank Dr. Jesse Smith for page proof reading. C.P. acknowledges Dr. H. Cynn from Lawrence

# Livermore National Laboratory for an illuminating discussion of the praseodymium phase transition.

- <sup>1</sup>G. Y. Shen, P. Chow, Y. M. Xiao, S. Sinogeikin, Y. Meng, W. G. Yang, H. P. Liermann, O. Shebanova, E. Rod, A. Bommannavar, and H. K. Mao, *High Pressure Res.* **28**, 145 (2008).
- <sup>2</sup>W. Uhoja, G. M. Tsoi, Y. K. Vohra, M. A. McGuire, A. S. Sefat, B. C. Sales, D. Mandrus, and S. T. Weir, *J. Phys.: Condens. Matter* **22**, 185702 (2010).
- <sup>3</sup>S. R. Li, Q. Li, K. Wang, X. Tan, M. Zhou, B. Li, B. B. Liu, G. T. Zou, and B. Zou, *J. Phys. Chem. B* **115**, 11816 (2011).
- <sup>4</sup>T. Yamanaka, A. Kyono, Y. Nakamoto, Y. Meng, S. Kharlamova, V. V. Struzhkin, and H. K. Mao, *Am. Mineral.* **98**, 736 (2013).
- <sup>5</sup>S. Hirai and W. L. Mao, *Appl. Phys. Lett.* **102**, 041912 (2013).
- <sup>6</sup>F. S. Elkin, I. P. Zibrov, A. P. Novikov, S. S. Khasanov, V. A. Sidorov, A. E. Petrova, T. A. Lograsso, J. D. Thompson, and S. M. Stishov, *Solid State Commun.* **181**, 41 (2014).
- <sup>7</sup>S. M. Wang, X. H. Yu, Z. J. Lin, R. F. Zhang, D. W. He, J. Q. Qin, J. L. Zhu, J. Han, L. Wang, H. K. Mao, J. Z. Zhang, and Y. S. Zhao, *Chem. Mater.* **24**, 3023 (2012).
- <sup>8</sup>Y. J. Wang, J. E. Panzik, B. Kiefer, and K. K. M. Lee, *Sci. Rep.* **2**, 520 (2012).
- <sup>9</sup>M. Derzsi, A. Budzianowski, V. V. Struzhkin, P. J. Malinowski, P. J. Leszczynski, Z. Mazej, and W. Grochala, *Crystengcomm* **15**, 192 (2013).
- <sup>10</sup>J. R. Jeffries, A. L. L. Sharma, P. A. Sharma, C. D. Spataru, S. K. McCall, J. D. Sugar, S. T. Weir, and Y. K. Vohra, *Phys. Rev. B* **84**, 092505 (2011).
- <sup>11</sup>J. G. Cheng, J. S. Zhou, J. B. Goodenough, H. D. Zhou, K. Matsubayashi, Y. Uwatoko, P. P. Kong, C. Q. Jin, W. G. Yang, and G. Y. Shen, *Phys. Rev. Lett.* **108**, 236403 (2012).
- <sup>12</sup>Z. Zhao, S. B. Wang, A. R. Oganov, P. C. Chen, Z. X. Liu, and W. D. L. Mao, *Phys. Rev. B* **89**, 180102 (2014).
- <sup>13</sup>W. G. Yang, F. J. Jia, L. Y. Tang, Q. Tao, Z. A. Xu, and X. J. Chen, *J. Appl. Phys.* **115**, 083915 (2014).
- <sup>14</sup>G. Tsoi, A. K. Stemshorn, Y. K. Vohra, P. M. Wu, F. C. Hsu, Y. L. Huang, M. K. Wu, K. W. Yeh, and S. T. Weir, *J. Phys.: Condens. Matter* **21**, 232201 (2009).
- <sup>15</sup>B. Kalisky, J. R. Kirtley, J. G. Analytis, J. H. Chu, A. Vailionis, I. R. Fisher, and K. A. Moler, *Phys. Rev. B* **81**, 184513 (2010).
- <sup>16</sup>J. Zhu, J. L. Zhang, P. P. Kong, S. J. Zhang, X. H. Yu, J. L. Zhu, Q. Q. Liu, X. Li, R. C. Yu, R. Ahuja, W. G. Yang, G. Y. Shen, H. K. Mao, H. M. Weng, X. Dai, Z. Fang, Y. S. Zhao, and C. Q. Jin, *Sci. Rep.* **3**, 2016 (2013).
- <sup>17</sup>P. P. Kong, F. Sun, L. Y. Xing, J. Zhu, S. J. Zhang, W. M. Li, Q. Q. Liu, X. C. Wang, S. M. Feng, X. H. Yu, J. L. Zhu, R. C. Yu, W. G. Yang, G. Y. Shen, Y. S. Zhao, R. Ahuja, H. K. Mao, and C. Q. Jin, *Sci. Rep.* **4**, 6679 (2014).
- <sup>18</sup>L. Wang, W. G. Yang, Y. Ding, Y. Ren, S. G. Xiao, B. B. Liu, S. V. Sinogeikin, Y. Meng, D. J. Gosztola, G. Y. Shen, R. J. Hemley, W. L. Mao, and H. K. Mao, *Phys. Rev. Lett.* **105**, 095701 (2010).
- <sup>19</sup>Q. S. Zeng, Y. Ding, W. L. Mao, W. G. Yang, S. V. Sinogeikin, J. F. Shu, H. K. Mao, and J. Z. Jiang, *Phys. Rev. Lett.* **104**, 105702 (2010).
- <sup>20</sup>X. J. Lu, Q. Y. Hu, W. G. Yang, L. G. Bai, H. Sheng, L. Wang, F. Q. Huang, J. G. Wen, D. J. Miller, and Y. S. Zhao, *J. Am. Chem. Soc.* **135**, 13947 (2013).
- <sup>21</sup>J. R. L. Mardegan, G. Fabbri, L. S. I. Veiga, C. Adriano, M. A. Avila, D. Haskel, and C. Giles, *Phys. Rev. B* **88**, 144105 (2013).
- <sup>22</sup>M. Somayazulu, P. Dera, A. F. Goncharov, S. A. Gramsch, P. Liermann, W. Yang, Z. Liu, H. K. Mao, and R. J. Hemley, *Nat. Chem.* **2**, 50 (2010).
- <sup>23</sup>M. Kim, M. Debessai, and C. S. Yoo, *Nat. Chem.* **2**, 784 (2010).
- <sup>24</sup>A. Vailionis, E. G. Gamaly, V. Mizeikis, W. G. Yang, A. V. Rode, and S. Juodkazis, *Nat. Commun.* **2**, 445 (2011).
- <sup>25</sup>B. Li, Y. Ding, W. G. Yang, L. Wang, B. Zou, J. F. Shu, S. Sinogeikin, C. Park, G. T. Zou, and H. K. Mao, *Proc. Natl. Acad. Sci. U. S. A.* **109**, 16459 (2012).
- <sup>26</sup>L. L. Sun, X. J. Chen, J. Guo, P. W. Gao, Q. Z. Huang, H. D. Wang, M. H. Fang, X. L. Chen, G. F. Chen, Q. Wu, C. Zhang, D. C. Gu, X. L. Dong, L. Wang, K. Yang, A. G. Li, X. Dai, H. K. Mao, and Z. X. Zhao, *Nature* **483**, 67 (2012).
- <sup>27</sup>W. W. Zhang, A. R. Oganov, A. F. Goncharov, Q. Zhu, S. E. Boulfelfel, A. O. Lyakhov, E. Stavrou, M. Somayazulu, V. B. Prakapenka, and Z. Konopkova, *Science* **342**, 1502 (2013).
- <sup>28</sup>Y. Ding, C. C. Chen, Q. S. Zeng, H. S. Kim, M. J. Han, M. Balasubramanian, R. Gordon, F. F. Li, L. G. Bai, D. Popov, S. M. Heald, T. Gog, H. K. Mao, and M. van Veenendaal, *Phys. Rev. Lett.* **112**, 056401 (2014).
- <sup>29</sup>M. Ahart, M. Somayazulu, R. E. Cohen, P. Ganesh, P. Dera, H. K. Mao, R. J. Hemley, Y. Ren, P. Liermann, and Z. G. Wu, *Nature* **451**, 545 (2008).
- <sup>30</sup>A. E. Gleason and W. L. Mao, *Nat. Geosci.* **6**, 571 (2013).
- <sup>31</sup>T. A. Strobel, M. Somayazulu, and R. J. Hemley, *Phys. Rev. Lett.* **103**, 065701 (2009).
- <sup>32</sup>D. Seoung, Y. Lee, H. Cynn, C. Park, K. Y. Choi, D. A. Blom, W. J. Evans, C. C. Kao, T. Vogt, and Y. Lee, *Nat. Chem.* **6**, 835 (2014).
- <sup>33</sup>G. Y. Shen, D. Ikuta, S. Sinogeikin, Q. Li, Y. Zhang, and C. F. Chen, *Phys. Rev. Lett.* **109**, 205503 (2012).
- <sup>34</sup>L. Bai, M. Pravica, Y. Zhao, C. Park, Y. Meng, S. V. Sinogeikin, and G. Shen, *J. Phys.: Condens. Matter* **24**, 435401 (2012).
- <sup>35</sup>C. L. Tracy, J. M. Pray, M. Lang, D. Popov, C. Park, C. Trautmann, and R. C. Ewing, *Nucl. Instrum. Methods Phys. Res., Sect. B* **326**, 169 (2014).
- <sup>36</sup>G. Shenoy, P. Viccaro, and D. M. Mills, *ANL Rep.* **88-9**, 2 (1992).
- <sup>37</sup>S. Narayanan, A. Sandy, D. Shu, M. Sprung, C. Preissner, and J. Sullivan, *J. Synchrotron Radiat.* **15**, 12 (2008).
- <sup>38</sup>B. X. Yang, M. Rivers, W. Schildkamp, and P. J. Eng, *Rev. Sci. Instrum.* **66**, 2278 (1995).
- <sup>39</sup>P. J. Eng, M. Newville, M. L. Rivers, and S. R. Sutton, *Proc. SPIE* **3449**, 145 (1998).
- <sup>40</sup>A. Hammersley, ESRF International Report No. ESRF98HA01T, 2004, program available at <http://www.esrf.eu/computing/scientific/FIT2D>.
- <sup>41</sup>J. Rodríguez-Carvajal, *Phys. Rev. B: Condens. Matter* **192**, 55 (1993).
- <sup>42</sup>R. A. Young, *The Rietveld Method* (Oxford University Press, 1995).
- <sup>43</sup>F. Gozzo, L. De Caro, C. Giannini, A. Guagliardi, B. Schmitt, and A. Prodi, *J. Appl. Crystallogr.* **39**, 347 (2006).
- <sup>44</sup>N. Ishimatsu, K. Matsumoto, H. Maruyama, N. Kawamura, M. Mizumaki, H. Sumiya, and T. Irifune, *J. Synchrotron Radiat.* **19**, 768 (2012).
- <sup>45</sup>A. Svane, W. M. Temmerman, Z. Szotek, J. Laegsgaard, and H. Winter, *Int. J. Quantum Chem.* **77**, 799 (2000).
- <sup>46</sup>M. J. Lipp, D. Jackson, H. Cynn, C. Aracne, W. J. Evans, and A. K. McMahan, *Phys. Rev. Lett.* **101**, 165703 (2008).
- <sup>47</sup>Y. Wang, L. G. Hector, H. Zhang, S. L. Shang, L. Q. Chen, and Z. K. Liu, *Phys. Rev. B* **78**, 104113 (2008).
- <sup>48</sup>W. M. Temmerman, A. Svane, Z. Szotek, H. Winter, and S. V. Beiden, in *Electronic Structure and Physical Properties of Solids: The Uses of the Lmto Method*, edited by H. Dreyse (Springer-Verlag Berlin, Berlin, 2000).
- <sup>49</sup>M. Casadei, X. G. Ren, P. Rinke, A. Rubio, and M. Scheffler, *Phys. Rev. Lett.* **109**, 146402 (2012).
- <sup>50</sup>M. Krisch, D. L. Farber, R. Xu, D. Antonangeli, C. M. Aracne, A. Beraud, T. C. Chiang, J. Zarestky, D. Y. Kim, E. I. Isaev, R. Ahuja, and B. Johansson, *Proc. Natl. Acad. Sci. U. S. A.* **108**, 9342 (2011).
- <sup>51</sup>M. J. Lipp, A. P. Sorini, J. Bradley, B. Maddox, K. T. Moore, H. Cynn, T. P. Devereaux, Y. Xiao, P. Chow, and W. J. Evans, *Phys. Rev. Lett.* **109**, 195705 (2012).
- <sup>52</sup>N. Lanata, Y. X. Yao, C. Z. Wang, K. M. Ho, J. Schmalian, K. Haule, and G. Kotliar, *Phys. Rev. Lett.* **111**, 196801 (2013).
- <sup>53</sup>H. Mao, R. Hazen, P. Bell, and J. Wittig, *J. Appl. Phys.* **52**, 4572 (1981).
- <sup>54</sup>B. J. Baer, H. Cynn, V. Iota, C.-S. Yoo, and G. Shen, *Phys. Rev. B* **67**, 134115 (2003).
- <sup>55</sup>B. Ravel and M. Newville, *J. Synchrotron Radiat.* **12**, 537 (2005).